

LOCAL REGULARITY ESTIMATION THROUGH SOBOLEV-SCALE NORM PROFILE *

XIAOBIN LI [†], LEEVAN LING[‡], AND YIZHONG SUN[§]

Abstract. We develop a kernel-based approach for estimating the spatially varying Sobolev regularity s of an unknown d -variate function f from scattered sampling data, which quantifies the degree of local differentiability supported by the data. Relying only on neighborhood data near the point of interest $z \in \Omega_z$, our method constructs a sequence of Sobolev-space reproducing kernel interpolants whose kernel smoothness order is specified by an index $m > d/2$. The native-space norms of these interpolants are evaluated over a bounded range of m , producing a *Sobolev-scale norm profile*. The elbow of this profile serves as a quantitative probe of the underlying local regularity $s(\Omega_z)$. In particular, when $m > s(\Omega_z)$, the profile exhibits rapid, near-worst-case growth governed by the classical upper bound associated with the conditioning of the kernel matrix. A band-limited surrogate analysis explains this transition and establishes a lower-bound relation linking native-norm growth to the Sobolev regularity of f . Two complementary strategies are incorporated for further enhancement: (i) a *stencil-shift* subroutine, which repositions local neighborhoods to avoid crossing discontinuities whenever possible, thereby suppressing artifacts in the norm estimates; and (ii) a local-global *norm-sweep comparison* strategy that combines short two-point local tails with an optional one-point global screen to detect outlier Ω_z of low Sobolev regularity and accelerate evaluation on large datasets. Numerical experiments on synthetic test functions and turbulent-flow data demonstrate accurate recovery of spatially varying regularity and confirm the robustness of the proposed characterization for kernel-based approximation and differentiation.

Key words. scattered data approximation, band-limited surrogate, local regularity, native norm, stencil-shift refinement

AMS subject classifications. 65M60, 65M12, 65D30, 41A30

1. Introduction. Estimating spatially varying smoothness from scattered data is a fundamental problem in numerical analysis and data-driven modeling. We consider an unknown d -variate function

$$f : \Omega \subset \mathbb{R}^d \rightarrow \mathbb{R}, \quad (X, f(X)) = \{(\mathbf{x}_i, f(\mathbf{x}_i))\}_{i=1}^N,$$

where $X \subset \Omega$ is a finite set of sampling locations. Given a point of interest $z \in \Omega$, we denote by Ω_z a small neighborhood containing z and by $X_z = X \cap \Omega_z$ the corresponding subset of samples. Our goal is to estimate the *local Sobolev regularity*

$$s = s(z) \quad \text{such that} \quad f \in H^{s(z)}(\Omega_z),$$

that is, the Sobolev order for which all weak derivatives $D^\alpha f$ with $|\alpha| < s(z)$ lie in $L_2(\Omega_z)$. The function $s(z)$ measures the degree of differentiability supported by the data near z , for example, a jump discontinuity admits $s < \frac{1}{2}$, while a corner or slope discontinuity yields $s < \frac{3}{2}$. Knowledge of $s(z)$ is valuable for detecting nonsmooth regions, selecting reconstruction stencils, and guiding adaptive solvers.

Traditional edge or singularity detection methods locate discontinuities via local peaks in interpolation coefficients or derivatives, often through polynomial or transform-based approaches such as ENO/WENO schemes, wavelet transforms, or

* Submitted to

Funding: This work was supported by the General Research Fund (GRF No. 12301021, 12300922, 12301824) of the Hong Kong Research Grants Council.

[†]Department of Mathematics, Hong Kong Baptist University (25481800@life.hkbu.edu.hk).

[‡]Department of Mathematics, Hong Kong Baptist University (lling@hkbu.edu.hk).

[§]Department of Mathematics, Hong Kong Baptist University (yzsun95@hkbu.edu.hk).

kernel filters [1, 2, 3, 4, 5, 6]. While classical wavelets [7] and high-order reconstructions like ENO/WENO [8, 9, 10] are highly effective on structured grids, their reliance on regular sampling and predesigned stencils limits their direct applicability to scattered or high-dimensional data. Moreover, these techniques yield mostly qualitative, often binary, indicators of smoothness rather than quantitative measures of differentiability.

Multiscale kernel constructions and samplet analysis provide complementary perspectives on localized approximation. Hierarchical and sparse-grid kernel schemes [11, 12, 13] introduce explicit multilevel structure into RBF approximation, enabling efficient representation of multiscale features on scattered data. In parallel, samplets [14, 15] combine the vanishing-moment property of wavelets with the geometric flexibility of meshfree methods. Constructed via hierarchical cluster trees, they form localized, distributional wavelets whose coefficients decay at rates governed by local smoothness. Recent studies further demonstrate that the samplet transform can compress and sparsify generalized Vandermonde matrices arising in multiscale RBF interpolation, particularly for globally supported kernels such as the Whittle-Matérn family [16]. This synergy unites the interpretability of wavelet-based analysis with the structural and modeling flexibility of kernel methods.

Despite these advances, most existing tools still focus on reconstructing or compressing multiscale information, rather than providing a direct, quantitative estimate of local Sobolev regularity from finite neighborhoods. Moreover, they typically process the entire dataset before identifying singular regions. In this paper, we propose a different approach: directly estimating Sobolev regularity from arbitrary local stencils of scattered samples via a *Sobolev-scale norm profile*. Section 2 defines this profile and introduces an elbow-based estimator of $s(\Omega_z)$. Section 3 develops the theoretical foundation linking native-norm growth to Sobolev regularity through Sobolev-native norm relations, band-limited surrogate analysis, and inverse inequalities. Section 4 presents refinement strategies, including the stencil-shift adjustment that reduces spatial smearing and the accelerated norm-sweep algorithm for quasi-uniform data. Finally, Section 5 shows numerical results on synthetic benchmarks and turbulent-flow data, demonstrating accurate and robust recovery of spatially varying Sobolev regularity.

2. Local regularity estimation via Sobolev-scale norm profiles. In many computational settings, measurements are available only at irregular locations, and the underlying field may exhibit nonsmooth features. Standard kernel interpolation methods often exhibit oscillatory behavior near such features. Rather than treating this instability as a numerical defect, we interpret it as diagnostic information about local loss of regularity.

This section introduces a kernel-based approach for quantifying local smoothness. The key idea is to examine, within each interior neighborhood, how the native norm of a kernel interpolant varies across a family of Sobolev-scale kernels. The resulting dependence on the kernel smoothness parameter m defines a local interpolant norm profile, which serves as a quantitative probe of the underlying regularity.

2.1. Preliminaries. We consider a family of translation-invariant, symmetric, positive definite (SPD) kernels $\{\Phi_m\}_{m>d/2}$ on \mathbb{R}^d , parameterized by the smoothness index m , where $\Phi_m(x, z) = \phi_m(\|x - z\|_2)$ for a radial function $\phi_m : [0, \infty) \rightarrow \mathbb{R}$. These kernels are characterized by the algebraic decay of their Fourier transforms,

$$(2.1) \quad c_1(1 + \|\omega\|_2^2)^{-m} \leq \widehat{\Phi}_m(\omega) \leq c_2(1 + \|\omega\|_2^2)^{-m}, \quad \omega \in \mathbb{R}^d,$$

for constants $0 < c_1 \leq c_2 < \infty$ that remain uniform over bounded intervals of $m > d/2$.

A standard example is the Whittle-Matérn kernel family,

$$(2.2) \quad \Phi_m(x, z) = \|x - z\|_2^{m-d/2} \mathcal{K}_{m-d/2}(\|x - z\|_2), \quad m > d/2,$$

where $\mathcal{K}_{m-d/2}$ denotes the modified Bessel function of the second kind. Its associated reproducing kernel Hilbert space (also called native space) $\mathcal{N}_{\Phi_m}(\mathbb{R}^d)$ is norm-equivalent to the Sobolev space $H^m(\mathbb{R}^d)$ [17, Thm. 10.47]. If a shape parameter $\varepsilon > 0$ is introduced via $\Phi_{m,\varepsilon}(x, z) = \Phi_m(\varepsilon\|x - z\|_2)$, this norm equivalence remains valid.

As in the introduction, let X_z denote the local neighborhood of data sites whose convex hull contains the evaluation point $z \in \Omega$. We record a few geometric quantities used in later analysis. The fill distance of X with respect to Ω_z and the separation distance of X are

$$(2.3) \quad h_{X, \Omega_z} := \sup_{x \in \Omega_z} \min_{x_j \in X} \|x - x_j\|_2, \quad q_X := \frac{1}{2} \min_{j \neq k} \|x_j - x_k\|_2,$$

and the local mesh ratio is $\rho_{X, \Omega_z} := h_{X, \Omega_z}/q_X$. From now on, we drop the subscript z and keep in mind that all data are local and located near z .

Let $Y = f|_X$ denote the data values of an unknown function f at the sites X . Associated with X , the finite-dimensional kernel trial space is

$$(2.4) \quad \mathcal{U}_{X, \Phi_m} := \text{span}\{\Phi_m(\cdot, x_j) : x_j \in X\}.$$

The interpolant $u_m \in \mathcal{U}_{X, \Phi_m}$ satisfies $u_m|_X = Y$ and can be written as

$$u_m(x) = \sum_{j=1}^n \alpha_j \Phi_m(x, x_j),$$

where the coefficient vector $\boldsymbol{\alpha}$ solves

$$\Phi_m(X, X) \boldsymbol{\alpha} = Y,$$

and $\Phi_m(X, X) \in \mathbb{R}^{n \times n}$ has entries $[\Phi_m(X, X)]_{jk} = \Phi_m(x_j, x_k)$. The native norm of the interpolant is then

$$(2.5) \quad \|u_m\|_{\mathcal{N}_{\Phi_m}}^2 = \boldsymbol{\alpha}^T \Phi_m(X, X) \boldsymbol{\alpha} = Y^T [\Phi_m(X, X)]^{-1} Y.$$

Equation (2.5) expresses the native norm purely through the data pair (X, Y) and the kernel order m . This quantity forms the basic building block of the interpolant norm profile introduced in the next subsection.

Although the interpolation condition $u_m|_X = Y$ holds for all m , the off-sample behavior of u_m depends strongly on the kernel smoothness. Larger m enforces higher smoothness and may produce Gibbs-type oscillations near nonsmooth regions, while a smaller m yields rougher approximants that can underfit smooth areas. Figure 1 illustrates this dependence and motivates examining the variation of the native norm with respect to m as an indicator of local regularity.

2.2. Sobolev-scale norm profile and data-driven regularity. To quantify local smoothness from scattered samples, we examine how the native norm of a kernel interpolant varies over the Sobolev scale. For each local stencil X with associated

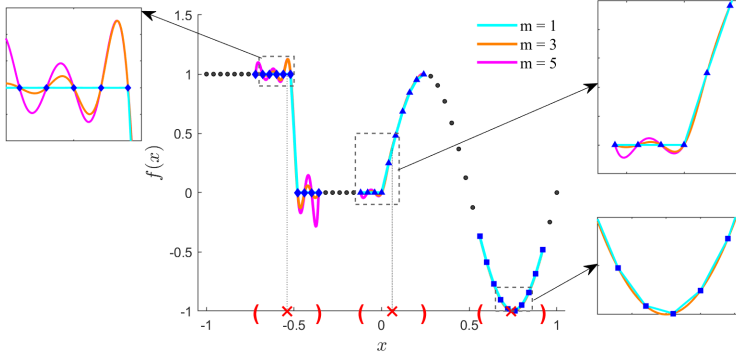


FIG. 1. One-dimensional RBF interpolation on local stencils using Whittle–Matérn kernels with smoothness $m = 1, 3, 5$. The test function is $f(x) = \sin(2\pi x)$ for $x > 0$, $f(x) = 0$ for $-0.5 < x \leq 0$, and $f(x) = 1$ for $-1 \leq x \leq -0.5$. A total of 51 sample points are used, and each local interpolant is computed on a stencil of 10 points.

function values Y in the neighborhood of an interior target z , we apply a local normalization so that the data vector Y has unit discrete ℓ_h^2 -norm. This normalization is performed separately for each stencil, making the resulting Sobolev-scale norm profile $\eta(m)$ (defined later in (2.6)) invariant to local amplitude and directly comparable across neighboring locations.

The diagnostic role of varying kernel smoothness was already illustrated in Figure 1. We consider the family of interpolants

$$u_m \in \mathcal{U}_{X, \Phi_m}, \quad m \in [m_{\min}, m_{\max}] \subset (d/2, \infty),$$

constructed for the data (X, Y) using the kernel interpolation method introduced in Section 2.1. Their native norms are evaluated as in (2.5), and we define the *Sobolev-scale norm profile* for z to be the native space norm of these interpolants:

$$(2.6) \quad \eta(m) := \|u_m\|_{\mathcal{N}_{\Phi_m}},$$

which depends only on the normalized data and on the kernel smoothness order m . The normalization removes amplitude effects so that $\eta(m)$ primarily reflects how the shape of the local samples interacts with the assumed smoothness order.

The maximal admissible growth of $\eta(m)$ can be bounded using the smallest eigenvalue of $\Phi_m(X, X)$ and the local separation distance q_X :

$$(2.7) \quad \eta(m) \leq \|Y\|_2 \lambda_{\min}^{-1/2}(\Phi_m(X, X)) \leq c_{m,d} \|Y\|_2 q_X^{d/2-m},$$

where $c_{m,d} > 0$ depends only on the kernel family and the dimension. This classical stability bound [18] provides a worst-case reference rate describing the steep regime of $\eta(m)$.

Figure 2 illustrates the upper bound (2.7) for one-dimensional functions with local regularity $s = 0.5, 1.5, 2.5$, and ∞ on uniformly spaced samples ($h = 2q_X$), where the asymptotic rate $q_X^{d/2-m}$ is well approximated by $(\pi/(2q_X))^{m-d/2}$. This follows from a simple one-dimensional heuristic: for evenly spaced nodes with spacing $h = 2q_X$, the largest representable frequency is $\omega_{\max} = \pi/(2q_X)$, so the proxy growth $\omega_{\max}^{m-d/2}$ yields exactly this approximation. Although such a Nyquist frequency does not exist for scattered data, one can estimate the smallest eigenvalues efficiently using power methods with low computational overhead.

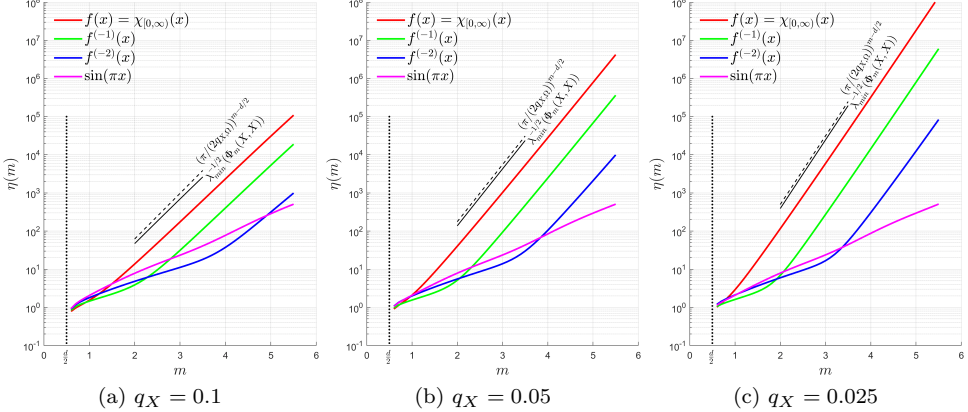


FIG. 2. Native-norm profiles $\eta(m)$ versus kernel smoothness m for RBF interpolants centered at $z = 0$, evaluated on local neighborhoods $\Omega_z = [-1, 1]$ constructed from point sets with separation distances $q_X = 0.1, 0.05$, and 0.025 . Colored curves correspond to a step function $f(x) = \chi_{[0, \infty)}(x)$, first- and second-order kink (given by the first and second antiderivatives $f^{(-1)}$ and $f^{(-2)}$ of f). Dashed and solid black lines show $\lambda_{\min}^{-1/2}(\Phi_m(X, X))$ and its approximation $(\pi/(2q_X))^{m-d/2}$, respectively, illustrating the worst-case rate in (2.7).

For lower regularity, where the true local order satisfies $s < m_{\min} \approx d/2$, the profile $\eta(m)$ grows immediately at the worst-case rate for all tested m , resulting in a nearly linear log-profile with no distinct elbow.

If $s \in [m_{\min}, m_{\max}]$, the profile $\eta(m)$ typically evolves through two regimes: for small m , the values vary moderately, whereas beyond a certain point they increase rapidly. Intuitively, if the underlying function is locally in H^s , then for $m < s$ the data remain compatible with the kernel space and the native norm stays nearly stable. Once $m > s$, the interpolant enforces excessive smoothness, causing $\eta(m)$ to grow quickly. On a semi-logarithmic scale $(m, \log \eta(m))$, this behavior forms an L-shaped curve: a flat region for $m \lesssim s$ followed by a steep, near power-law rise for $m \gtrsim s$, close to the worst-case rate (2.7). We identify the corner of this transition as a surrogate for the largest Sobolev order detectable from the samples and define the corresponding *L-curve elbow* via the curvature of the log-norm curve:

$$(2.8) \quad m^* = \arg \max_m \frac{|(\log \eta(m))''|}{(1 + ((\log \eta(m))')^2)^{3/2}}.$$

For smooth data, where $s > m_{\max}$, the profile $\eta(m)$ also grows almost linearly in the log-scale but at a significantly slower rate with respect to (2.7).

DEFINITION 2.1 (Data-driven regularity). *Let $\eta(m)$ denote the Sobolev-scale norm profile evaluated over a prescribed interval of Sobolev orders $[m_{\min}, m_{\max}]$, and m^* be the elbow defined in (2.8). Then, the data-driven regularity $\tilde{s}(\Omega_z)$ is defined by*

1. $\tilde{s}(\Omega_z) = m^*$, if a distinct elbow¹ is present;

¹A *distinct elbow* refers to a point m^* at which the log-norm profile $(m, \log \eta(m))$ exhibits a clear change of slope, in the sense that the difference between the local pre- and post-elbow slopes exceeds a chosen contrast threshold (typically several times the numerical slope variation within each region). In practice, this corresponds to a visually discernible transition between the mild- and rapid-growth regimes of $\eta(m)$.

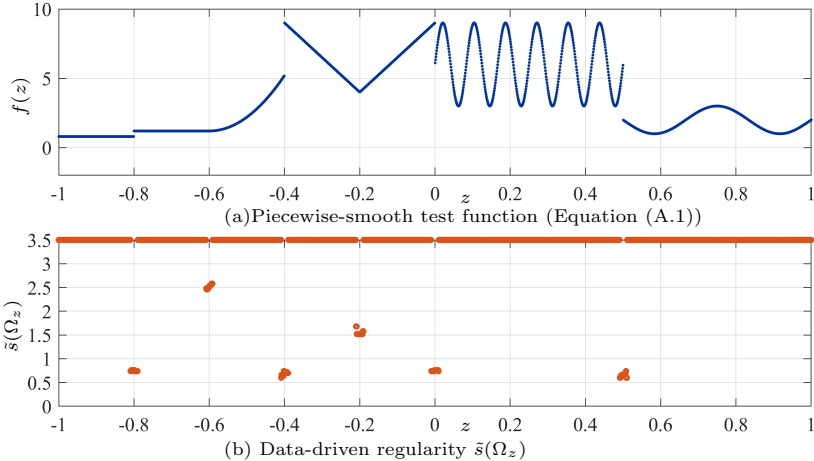


FIG. 3. Native-norm profiles $\eta(m)$ are evaluated for $m \in [0.6, 3.5]$ with step size $\Delta m = 0.025$ on local neighborhoods of size 20 (total 2000 samples). The elbow location $\tilde{s}(\Omega_z)$ is extracted from the discrete curvature of the log-profile (2.8). The resulting spatial map shows pronounced drops near nonsmooth regions, indicating reduced local Sobolev regularity.

2. $\tilde{s}(\Omega_z) = m_{\min}$, if the profile is nearly linear with slope comparable to the worst case rate (2.7);
3. $\tilde{s}(\Omega_z) = m_{\max}$, if the profile is nearly linear with slope significantly smaller than the worst case rate (2.7).

A theoretical justification for this procedure is developed later in Section 3 using Sobolev–native norm relations and band-limited surrogate estimates.

Figure 3 illustrates this procedure for a piecewise-smooth function (A.1) defined in Appendix A containing several singular features. The recovered field m^* , and its interpretation as the data-driven regularity $\tilde{s}(\Omega_z)$, provides a sharp quantitative indicator of spatially varying smoothness. In this example, the data-driven regularity $\tilde{s}(\Omega_z)$ distinguishes different types of singular behavior: near jump discontinuities $\tilde{s}(\Omega_z) \gtrsim 0.5$; around corners (integrals of jumps) $\tilde{s}(\Omega_z) \gtrsim 1.5$; and after a second integration $\tilde{s}(\Omega_z) \gtrsim 2.5$. Although the last case ($s = 2.5$) may appear visually smooth, the native-norm profile $\eta(m)$ reveals its limited local regularity. A slight overestimation of $\tilde{s}(\Omega_z)$ is expected, since the analysis is based on discrete samples. A more detailed discussion of this effect is provided in Section 3.

3. Band-limited Analysis of the Sobolev-scale Norm Profile. The construction in the previous section, where the data-driven regularity $\tilde{s}(\Omega_z)$ was introduced through the curvature of the Sobolev-scale norm profile $\eta(m)$, was based on the empirical observation that $\eta(m)$ approximately follows the upper envelope (2.7). To complete the theoretical picture, we now seek a complementary *lower bound* for $\eta(m)$ that characterizes its minimal growth for functions of a given Sobolev regularity s . Deriving such a bound is nontrivial, since it must hold for all $f \in H^s$, including arbitrarily smooth functions. To this end, we introduce a band-limited surrogate formulation that captures the essential spectral content of Sobolev functions while enabling explicit comparison between Sobolev and native norms. This band-limited analysis provides a quantitative lower bound on $\eta(m)$ and forms the theoretical foundation for the main theorem presented below.

3.1. Spectral Median of Band-limited Functions. We work in the Fourier-defined (Bessel-potential) Sobolev spaces. For any $m \geq 0$ and any $g \in L^2(\mathbb{R}^d)$, define

$$(3.1) \quad \|g\|_{H^m(\mathbb{R}^d)}^2 := \int_{\mathbb{R}^d} (1 + \|\omega\|^2)^m |\widehat{g}(\omega)|^2 d\omega,$$

which is well-defined also for fractional m .

Given a cutoff $\sigma > 0$, define the band-limited space $\mathcal{B}_\sigma := \{f_\sigma \in L^2(\mathbb{R}^d) : \text{supp } \widehat{f}_\sigma \subseteq B(0, \sigma)\}$. Thus, \mathcal{B}_σ consists of all functions whose Fourier transforms vanish outside the ball of radius σ centered at the origin. To describe how the H^m -norm of a band-limited function is distributed across frequencies near the spectral cutoff, we introduce a balance parameter called the *spectral median*.

DEFINITION 3.1 (Spectral median). *Let $f_\sigma \in \mathcal{B}_\sigma$ and $t > 0$. For $\theta \in [0, 1]$, define the spectral shell $\mathcal{S}_{\theta, \sigma} := \{\omega \in \mathbb{R}^d : \theta \leq \|\omega\|/\sigma \leq 1\}$. The spectral median of f_σ is defined as*

$$(3.2) \quad \beta_t(f_\sigma) := \max \left\{ \theta \in [0, 1] : \int_{\mathcal{S}_{\theta, \sigma}} (1 + \|\omega\|^2)^t |\widehat{f}_\sigma(\omega)|^2 d\omega \geq \frac{1}{2} \|f_\sigma\|_{H^t(\mathbb{R}^d)}^2 \right\}.$$

Therefore, the spectral median identifies the largest normalized cutoff $\beta_t \in [0, 1]$ such that the highpass region $\mathcal{S}_{\beta_t(f_\sigma), \sigma}$ still contributes at least half of the H^t -norm of f_σ . The maximizer in (3.2) uniquely exists by monotonicity and boundedness of the function $\theta \mapsto \int_{\mathcal{S}_{\theta, \sigma}} (1 + \|\omega\|^2)^t |\widehat{f}_\sigma(\omega)|^2 d\omega$. In particular, $\beta_m(f_\sigma)$ is defined uniquely even when \widehat{f}_σ has support of measure zero (e.g. a single frequency). For continuous spectra, β_m simply represents the smallest highpass band carrying half of the H^m energy.

The next result shows that the growth of Sobolev norms with respect to the order m is bounded from below by the spectral median and a lower-order Sobolev norm.

LEMMA 3.2. *For any $f_\sigma \in \mathcal{B}_\sigma(\mathbb{R}^d)$ and $0 < s < m$, we have*

$$(3.3) \quad \|f_\sigma\|_{H^m(\mathbb{R}^d)} \geq \|f_\sigma\|_{H^s(\mathbb{R}^d)} \exp \left(\frac{1}{4} \int_s^m \log(1 + (\beta_t(f_\sigma)\sigma)^2) dt \right).$$

Proof. If $f_\sigma \equiv 0$ the claim is trivial. For $f_\sigma \neq 0$, fix any $t \in [s, m]$. We begin with the logarithmic derivative of the squared Sobolev norm,

$$(3.4) \quad \frac{d}{dt} \log \|f_\sigma\|_{H^t(\mathbb{R}^d)}^2 = \|f_\sigma\|_{H^t(\mathbb{R}^d)}^{-2} \left(\frac{d}{dt} \|f_\sigma\|_{H^t(\mathbb{R}^d)}^2 \right).$$

The derivative of $\|f_\sigma\|_{H^t}^2$ with respect to t is

$$(3.5) \quad \frac{d}{dt} \|f_\sigma\|_{H^t(\mathbb{R}^d)}^2 = \int_{\|\omega\| \leq \sigma} (1 + \|\omega\|^2)^t |\widehat{f}_\sigma(\omega)|^2 \log(1 + \|\omega\|^2) d\omega.$$

Combining (3.4) and (3.5) gives

$$\frac{d}{dt} \log \|f_\sigma\|_{H^t(\mathbb{R}^d)}^2 = \|f_\sigma\|_{H^t(\mathbb{R}^d)}^{-2} \int_{\|\omega\| \leq \sigma} (1 + \|\omega\|^2)^t |\widehat{f}_\sigma(\omega)|^2 \log(1 + \|\omega\|^2) d\omega.$$

For simplicity, write $\beta_t = \beta_t(f_\sigma)$. Restrict the integral in (3.5) to the high-pass region $\mathcal{S}_{\beta_t, \sigma}$; applying the defining condition (3.2) for β_t gives

$$\begin{aligned} \frac{d}{dt} \log \|f_\sigma\|_{H^t(\mathbb{R}^d)}^2 &\geq \|f_\sigma\|_{H^t(\mathbb{R}^d)}^{-2} \int_{\mathcal{S}_{\beta_t, \sigma}} (1 + \|\omega\|^2)^t |\widehat{f}_\sigma(\omega)|^2 \log(1 + \|\omega\|^2) d\omega \\ &\geq \log(1 + (\beta_t \sigma)^2) \|f_\sigma\|_{H^t(\mathbb{R}^d)}^{-2} \int_{\mathcal{S}_{\beta_t, \sigma}} (1 + \|\omega\|^2)^t |\widehat{f}_\sigma(\omega)|^2 d\omega, \end{aligned}$$

where the second line uses that $\log(1 + \|\omega\|^2) \geq \log(1 + (\beta_t \sigma)^2)$ for every $\omega \in \mathcal{S}_{\beta_t, \sigma}$. By using the half-energy property (3.2), we obtain

$$(3.6) \quad \frac{d}{dt} \log \|f_\sigma\|_{H^t(\mathbb{R}^d)} \geq \frac{1}{4} \log(1 + (\beta_t \sigma)^2).$$

Integrating (3.6) with respect to t over the interval $[s, m]$ completes the proof. \square

3.2. Lower Bound for the Sobolev-Scale Norm Profile. We begin by recalling that the existence and basic approximation properties of band-limited interpolants are well established [18, Section 3]. Let $m, t > 0$ with $d/2 < t \leq m$, and let $\Omega \subset \mathbb{R}^d$ be a bounded Lipschitz domain equipped with a continuous extension operator $E_\Omega : H^m(\Omega) \rightarrow H^m(\mathbb{R}^d)$. For any $u \in H^m(\Omega)$ and $\sigma = \kappa_{t,d} q_{X,\Omega}^{-1}$ with $\kappa_{t,d}$ chosen sufficiently large, there exists a band-limited function $f_{\sigma,u,t,\Omega} \in \mathcal{B}_\sigma$ that interpolates the data on X , i.e. $u|_X = f_{\sigma,u,t,\Omega}|_X$, and satisfies the uniform stability and approximation bounds

$$(3.7a) \quad \|f_{\sigma,u,t,\Omega}\|_{H^t(\mathbb{R}^d)} \leq C \|u\|_{H^t(\Omega)},$$

$$(3.7b) \quad \|u - f_{\sigma,u,t,\Omega}\|_{H^t(\Omega)} \leq C' q_{X,\Omega}^{m-t} \|u\|_{H^m(\Omega)}.$$

For each $t \in [s, m]$, we introduce a canonical representative chosen to minimize the H^t norm subject to the interpolation constraints:

$$(3.8) \quad f_{\sigma,t,X,Y}^* := \arg \min \left\{ \|f_\sigma\|_{H^t(\mathbb{R}^d)} : f_\sigma \in \mathcal{B}_\sigma(\mathbb{R}^d), f_\sigma|_X = Y \right\}.$$

Existence and uniqueness of $f_{\sigma,t,X,Y}^*$ follow from the strict convexity of the Sobolev norm on the affine subspace of \mathcal{B}_σ defined by the interpolation conditions. The mapping $t \mapsto f_{\sigma,t,X,Y}^*$ is continuous, and as t increases, the weight $(1 + \|\omega\|^2)^t$ in the Fourier norm progressively emphasizes the higher frequencies already present below σ . Once all degrees of freedom permitted by the data and the band-limit have been activated, no further smoothing is possible, and the family $\{f_{\sigma,t,X,Y}^*\}_{t>0}$ stabilizes to a limiting element $f_{\sigma,\infty,X,Y}$ within the same affine space. See Figure 4 for a schematic illustration.

We now relate the kernel interpolant $u_m \in \mathcal{U}_{X,\Phi_m}$ to the band-limited interpolants introduced above. For each $m \in [m_{\min}, m_{\max}]$, let the bandwidth parameter $\sigma = \kappa_{m,d} q_{X,\Omega}^{-1}$, where $\kappa_{m,d}$, depending only on m and d , is chosen sufficiently large to guarantee the existence of a band-limited surrogate $f_{\sigma,u_m,m,\Omega} \in \mathcal{B}_\sigma(\mathbb{R}^d)$ satisfying $f_{\sigma,u_m,m,\Omega}|_X = u_m|_X = Y$ and the uniform stability bound

$$(3.9) \quad \|f_{\sigma,u_m,m,\Omega}\|_{H^m(\mathbb{R}^d)} \leq C_m \|u_m\|_{H^m(\Omega)}.$$

To treat all $m \in [m_{\min}, m_{\max}]$ simultaneously, we fix

$$\kappa_d := \max_{m \in [m_{\min}, m_{\max}]} \kappa_{m,d}, \quad C := \max_{m \in [m_{\min}, m_{\max}]} C_m,$$

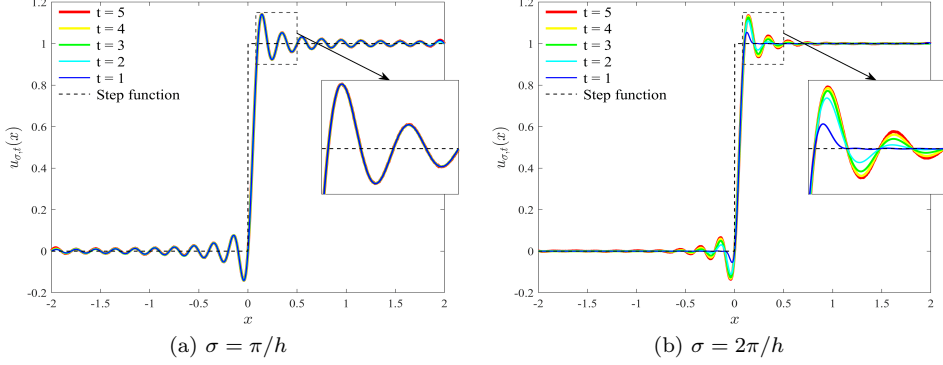


FIG. 4. Band-limited kernel interpolation of the one-dimensional step function $f(x) = \chi_{(0,\infty)}(x)$ from uniformly spaced samples. The interpolants $u_{\sigma,t}$ use Fourier-domain kernels $\hat{\Phi}_{\sigma,t}(\omega) = (1 + \omega^2)^{-t} \mathbf{1}_{|\omega| \leq \sigma}$, with $t = 1, \dots, 5$. The Fourier-truncated kernel is used here solely to illustrate the band-limited surrogate viewpoint and the stabilization of the interpolant as t increases.

thereby ensuring that (3.9) holds uniformly for all m with the common bandwidth $\sigma = \kappa_d q_{X,\Omega}^{-1}$. Next, we note that the equivalence constant between the native and Sobolev norms for Sobolev reproducing kernels is independent of m .

LEMMA 3.3. *Assume Φ_m ($m > d/2$) satisfies the Fourier decay condition (2.1) with upper-bound constant c_2 . Then there exists a constant $C_{d,c_2} > 0$, depending only on d , such that*

$$(3.10) \quad \|v\|_{\mathcal{N}_{\Phi_m}} \geq C_{d,c_2} \|v\|_{H^m(\mathbb{R}^d)}, \quad \text{for all } v \in \mathcal{N}_{\Phi_m}(\mathbb{R}^d).$$

Proof. The claim follows directly from the Fourier decay assumption (2.1) and the standard Fourier characterization of native spaces (see, e.g., [17, Cor. 10.48]). \square

Combining (3.9) and (3.10) gives

$$(3.11) \quad \eta(m) := \|u_m\|_{\mathcal{N}_{\Phi_m}} \gtrsim \|u_m\|_{H^m(\Omega)} \gtrsim \|f_{\sigma,u_m,m,\Omega}\|_{H^m(\mathbb{R}^d)}.$$

By definition of the optimal band-limited interpolant $f_{\sigma,m,X,Y}^*$ in (3.8), its H^m -norm is minimal among all band-limited functions matching the data; hence, there exists a constant C_0 such that the following holds:

$$(3.12) \quad \eta(m) \geq C_0 \|f_{\sigma,m,X,Y}^*\|_{H^m(\mathbb{R}^d)}, \quad \text{for all } m \in [m_{\min}, m_{\max}].$$

Thus, the kernel-based norm profile $\eta(m)$ is bounded below by the family of minimal-norm band-limited interpolants $f_{\sigma,m,X,Y}^*$. We are now ready to apply Lemma 3.2 to $f_{\sigma,m,X,Y}^*$ and establish the quantitative lower bound leading to the main theorem.

THEOREM 3.4. *Let $\{\Phi_m\}_{m \in [m_{\min}, m_{\max}]}$ be a family of admissible kernels on \mathbb{R}^d such that, for each $m > d/2$, the associated native space \mathcal{N}_{Φ_m} is norm-equivalent to the Sobolev space $H^m(\mathbb{R}^d)$. For each $m \in [m_{\min}, m_{\max}]$, let $u_m \in \mathcal{U}_{X,\Phi_m}$ be the kernel interpolant satisfying $u_m|_X = Y$, and define $\eta(m) := \|u_m\|_{\mathcal{N}_{\Phi_m}}$. Let $s > 0$ be a fixed reference Sobolev order and set $s_* := \min\{s, m\}$. For $\sigma = \kappa q_X^{-1}$ with some sufficiently large fixed $\kappa > 0$, let $f_{\sigma,t,X,Y}^*$ denote the minimal-norm band-limited interpolants defined in (3.8). Then there exists a constant $C > 0$, independent of X ,*

Y , and $m \in [m_{\min}, m_{\max}]$, such that

$$(3.13) \quad \eta(m) \geq C \|f_{\sigma, s_*, X, Y}^*\|_{H^{s_*}(\mathbb{R}^d)} \exp\left(\frac{1}{4} \int_{s_*}^m \log\left(1 + (\beta_t(f_{\sigma, m, X, Y}^*) \sigma)^2\right) dt\right),$$

where, for each $t \in [s_*, m]$, $\beta_t(\cdot)$ denotes the spectral median as defined in (3.2).

The parameter s quantifies the *a priori* Sobolev regularity of the unknown target function f generating the data $Y = f|_X$. In this context, the term $\|f_{\sigma, s, X, Y}^*\|_{H^s(\mathbb{R}^d)}$ serves as a quantifiable surrogate for $\|f\|_{H^s(\Omega)}$, representing the best achievable H^s -approximation from the family of band-limited interpolants. The theorem thereby establishes a direct link between the native-space norm profile $\eta(m)$ of the kernel interpolants and the smoothness profile of an underlying function of regularity s .

The lower bound (3.13) highlights two effects: the prefactor $\|f_{\sigma, s_*, X, Y}^*\|_{H^{s_*}}$ measures the minimal band-limited energy of the data at order s_* , while the exponential factor captures growth in higher-order Sobolev norms when a significant portion of the spectrum lies near the cutoff σ . For interpretation, take $s = s(z)$ as a local Sobolev benchmark. If $m \leq s(z)$, then $s_* = m$ and the exponential term is inactive, so $\eta(m)$ grows only mildly with m . For $m > s(z)$, the integral activates, and $\beta_t(f_{\sigma, m, X, Y}^*)$ drives a rapid increase of $\eta(m)$, producing the observed “elbow” in $(m, \log \eta(m))$. For sufficiently large m , $f_{\sigma, m, X, Y}^*$ stabilizes and $\beta_t \rightarrow \beta_\infty$, so the integral grows linearly in m and the slope of $\log \eta(m)$ saturates, as illustrated in Figure 2.

Proof. If $m \leq s$, then $s_* = m$, and the exponential term in (3.13) reduces to 1. In this case, the estimate follows directly from the basic inequality (3.12), up to a constant factor. If $m > s$, we must compare the kernel norm at order m with the H^s -norm of the band-limited interpolant. Applying Lemma 3.2 to $f_\sigma = f_{\sigma, m, X, Y}^*$ with lower order $s_* = s$ and using the minimality of $f_{\sigma, s, X, Y}^*$ in H^s gives (3.13). Thus, $s_* = \min\{s, m\}$ simply ensures that the bound stops at the smaller of the available regularities: if the data-generating function is smoother ($s > m$), the estimate uses its H^m -norm; otherwise, it uses its H^s -norm. \square

4. Optional extensions: stencil refinement and fast norm sweeps. This section presents two independent, practical extensions of the framework: (i) a *stencil-shift refinement* that tests a small set of nearby stencil positions to improve spatial localization of low-regularity features, and (ii) a local-and-global accelerated norm-sweep that estimates $\eta(m)$ on large datasets using a two-point local tail for each neighborhood, optionally combined with a one-point global screen for further speedup.

4.1. Stencil-shift for sharper localization. The data-driven regularity $\tilde{s}(\Omega_z)$ in Definition 2.1 is computed on a neighborhood Ω_z centered at an evaluation point z . When Ω_z crosses an interface or a steep transition, its samples may contain both smooth and nonsmooth components. In such cases, the data-driven regularity $\tilde{s}(\Omega_z) < m_{\max}$ tends to reflect the rougher side, even when z itself lies within a smoother subregion. This can lead to spatial smearing, where low-regularity estimates extend across nearby points whose neighborhoods intersect the same feature.

To alleviate this effect, we test several nearby stencil positions and retain the one that yields a higher regularity estimate. Whenever $\tilde{s}(\Omega_z) < m_{\max}$, the neighborhood is considered contaminated by low-regularity samples. A small collection of alternative neighborhoods $\{\Omega'_z\}$ is then created by locally shifting the stencil center while preserving the interpolatory geometry. For each candidate Ω'_z , the norm profile $\eta(m)$ is recomputed, and the corresponding data-driven regularity $\tilde{s}(\Omega'_z)$ is evaluated. The

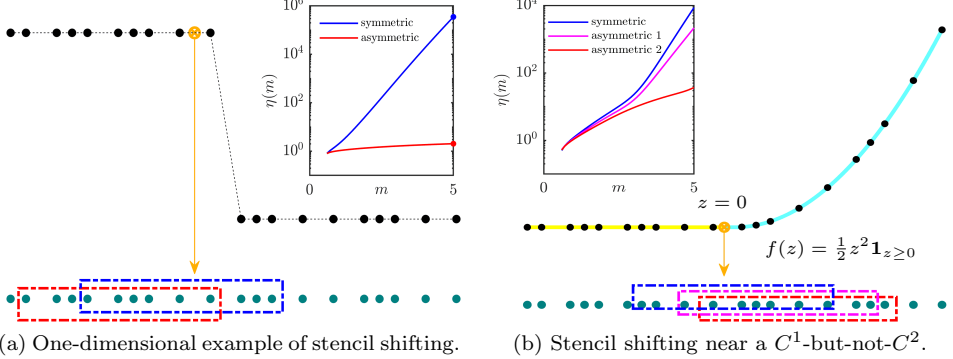


FIG. 5. (a) A symmetric stencil spanning a discontinuity produces an underestimated data-driven regularity $\tilde{s}(\Omega_z)$. Shifting the stencil slightly away from the jump avoids mixed samples, leading to a higher $\tilde{s}(\Omega_z)$ and sharper localization of the smooth region. (b) The test function is $f(z) = \frac{1}{2}z^2 \mathbf{1}_{z \geq 0}$ and the target location is $z = 0$, taken as an off-sample point ($z \notin X$). Different shifted neighborhoods yield markedly different norm profiles $\eta(m)$. In the extreme case where the shifted stencil becomes highly one-sided and the center approaches the stencil boundary (red), the profile can appear artificially mild, leading to an overestimation of the local regularity \tilde{s} under Definition 2.1. This motivates the interior admissibility constraint used in the stencil-shift procedure.

final regularity value at z is updated as

$$\tilde{s}(\Omega_z) := \max_{\Omega'_z \in \mathcal{N}(z)} \tilde{s}(\Omega'_z),$$

where $\mathcal{N}(z)$ denotes the set of admissible shifted neighborhoods. Figure 5a illustrates the idea in one dimension: a symmetric stencil spanning a discontinuity corresponds to case 2 in Definition 2.1, whereas a slight lateral shift avoids mixed samples and produces a flatter $\log \eta(m)$ profile with a smaller slope, corresponding to case 3.

In higher dimensions, the candidate shifts are constructed geometrically. Starting from the symmetric stencil X_z^{sym} , we identify a stable core $\mathcal{C}_z \subseteq X_z^{\text{sym}}$ and its convex hull $\text{conv}(\mathcal{C}_z)$ around z (Figure 6), which defines the region where interpolation remains well conditioned. Candidate shift directions are drawn from (i) rays connecting z to the hull vertices and (ii) outward normals to hull edges in two dimensions or to hull faces in three dimensions (Figure 7).

For each direction v_k , we construct a few trial offsets $z + r v_k$, $r \in [0, r_{\max}(z)]$. Each offset defines a circular (in 2D) or spherical (in 3D) region $\mathcal{B}(z + r v_k, \rho_z)$ of radius ρ_z , matching the local stencil radius of Ω_z . New neighborhoods $\Omega'_z(r)$ are obtained by selecting the n nearest samples to the shifted center within $\mathcal{B}(z + r v_k, \rho_z)$. A key caveat is that overly aggressive shifts may produce stencils that become geometrically one-sided (or otherwise under-informative) with respect to a nearby limited-regularity feature. In this situation, the shifted neighborhood may contain too few samples across the feature to reliably reflect the local loss of regularity. Consequently, the tail of the $\log \eta(m)$ profile can appear artificially mild, leading to an overestimation of the local regularity under Definition 2.1. To mitigate this effect, each candidate should satisfy the interior condition

$$\text{dist}(z, \partial \text{conv}(\mathcal{C}_z)) \geq c q_{X_z},$$

where q_{X_z} is the local spacing and $c > 0$ is a user-chosen safety factor. Figure 5b provides a demo of this failure mode for a function that is locally C^1 but not C^2 . Here the target location is $z = 0$, which is an off-sample point (i.e., $z \notin X$). Depending

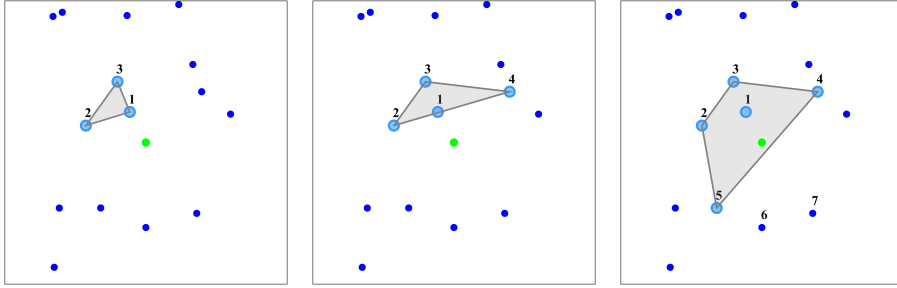


FIG. 6. Convex-hull construction around the evaluation point z . The admissibility condition $\text{dist}(z, \partial \text{conv}(\mathcal{C}_z)) \geq c q_{X_z}$ prevents shifted centers from approaching the hull boundary, which would lead to ill-conditioned interpolation neighborhoods.

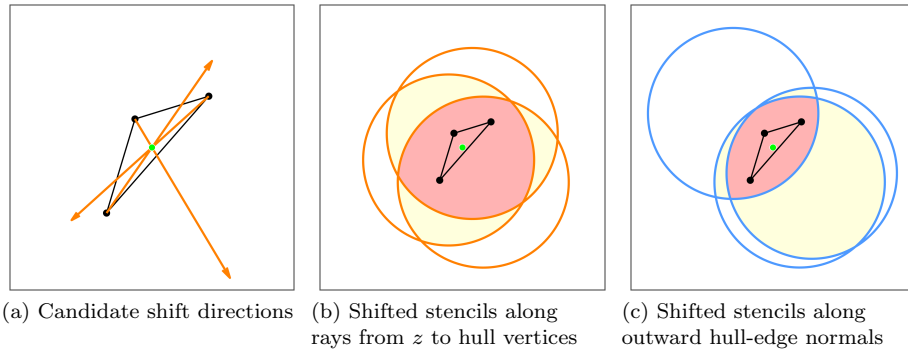


FIG. 7. Candidate shift directions in two dimensions, generated from the convex-hull geometry. Each trial offset defines a circular region used to form a shifted neighborhood.

on the shift, the norm profile may either indicate limited regularity or lead to an overestimated regularity under Definition 2.1. If the target point were included as a data site (i.e., $z \in X$), this overestimation is not observed in this demo.

The stencil-shift procedure uses only geometric information from the local sample distribution and operates independently at each z . It suppresses spurious low-regularity detections near interfaces, narrows smeared transition zones, and improves the spatial localization of the data-driven regularity $\tilde{s}(\Omega_z)$. In addition, it can also serve as a geometric prefilter for constructing RBF-FD or other meshfree stencils that preserve interpolation accuracy while avoiding cross-feature sampling.

4.2. Accelerated norm sweeps on large datasets. A dense evaluation of the Sobolev-scale native-norm profile $\eta(m)$ at many m -values for every point z quickly becomes intractable on large datasets. In practice, only the high- m portion of the curve is needed to estimate the local data-driven regularity. The procedure below achieves that using at most two norm evaluations per point, keeping the computation entirely local.

For each z , we evaluate $\eta(m)$ only at the two highest available orders,

$$m_1 = m_{\max} - \delta, \quad m_2 = m_{\max},$$

where m_{\max} is the upper boundary of the tested kernel orders and $\delta > 0$ is a small fixed step within the stable range. The pair $\{\eta(m_1), \eta(m_2)\}$ provides a short secant

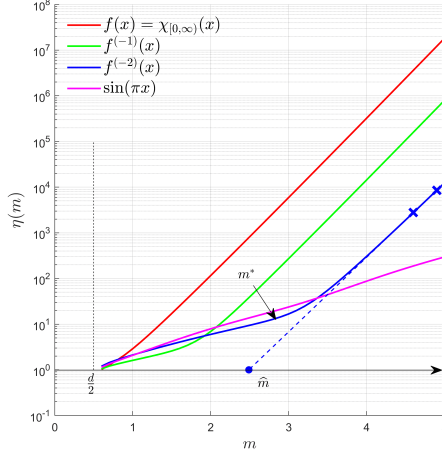


FIG. 8. Two-point tail estimation of $\tilde{s}(\Omega_z)$. Each log-profile $\log \eta(m)$ is sampled only at $m_1 = m_{\max} - \delta$ and $m_2 = m_{\max}$. If the slope at m_{\max} grows significantly slower than the worst-case trend, the neighborhood is considered locally smooth. Otherwise, the secant between these two points approximates the high- m tail, and its intersection with $\log \eta = 0$ gives an elbow-free transition estimate \hat{m} . An optional one-point global screening step can further restrict such evaluations to outlier neighborhoods.

segment of the log-profile $\log \eta(m)$ near its high- m end. If the local slope at m_{\max} is substantially smaller than that of the steep, worst-case growth in (2.7), the neighborhood is considered locally smooth and we assign $\tilde{s}(\Omega_z) \approx m_{\max}$. Otherwise, the two samples define a descending secant line that approximates the local tail of $\log \eta(m)$. The intersection of this line with $\log \eta = 0$ yields a simple lower estimate to the elbow,

$$\hat{m}(z) = m_2 - \frac{\log \eta(m_2)}{\text{slope}(m_1, m_2)},$$

which serves as the approximate elbow for that neighborhood, see Figure 8. This estimate reflects how quickly the high-order native norm departs from smooth scaling and requires only two kernel solves per point. The resulting scheme remains entirely local, uses at most two norm evaluations per neighborhood, and eliminates the need for dense m -sweeps or explicit elbow detection. Detected low-regularity candidates can later be refined geometrically through the stencil-shift process of Section 4.1.

For even larger datasets, we can include an optional global screening stage to reduce the number of these two-point evaluations. In this variant, we first compute a single high-order value $\eta(m_{\max})$ at all $z \in Z$. Points whose $\log \eta(m_{\max})$ appear as outliers in the global distribution are collected into a reduced set Z_o . This detection can, for example, use a robust interquartile-range (IQR) rule. The local two-point secant refinement is then applied only to Z_o , while other points retain $\tilde{s}(\Omega_z) \approx m_{\max}$ by default. This optional one- m screening provides an additional order-of-magnitude speed-up with minimal loss of accuracy. The same screening strategy can also be combined with the stencil-shift refinement in subsection 4.1, as illustrated in Figure 5a.

5. Numerical examples. This section demonstrates the proposed Sobolev-scale norm profiling procedure on one- and two-dimensional scattered datasets, including synthetic test functions and a turbulent-flow case. The first two examples examine parameter effects in one dimension, followed by two-dimensional and turbulent-flow applications in later subsections.

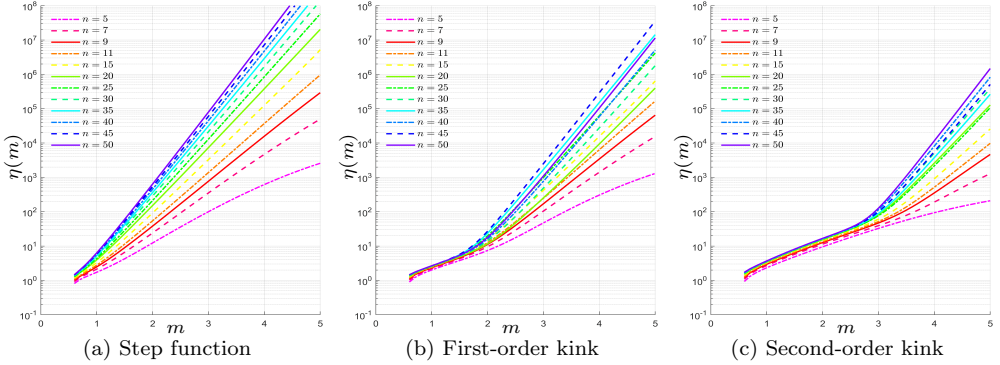


FIG. 9. (**Example 1**) Discrete native-norm profiles $\eta(m)$ for three one-dimensional test functions (a step function, a first-order kink, and a second-order kink), corresponding to Sobolev regularities $H^{0.5-}$, $H^{1.5-}$, and $H^{2.5-}$, respectively. A Whittle-Matérn kernel with $\varepsilon = 1$ is used on $\Omega = [-0.5, 0.5]$. Each curve corresponds to a different stencil size n ranging from 5 to 50.

The local analysis estimates the data-driven regularity order $\tilde{s}(\Omega_z)$ from neighborhood samples and investigates how $\tilde{s}(\Omega_z)$ approaches the intrinsic scale $s(\Omega_z)$ as the sampling is refined or kernel parameters are varied. In all examples, the Whittle-Matérn kernel family defined in (2.2) is used, with the shape parameter ε specified individually and smoothness index $m \in (d/2, 5]$ swept to form the discrete norm profile $\eta(m)$.

5.1. Example 1: Stencil-size dependence in one dimension. We first study how the data resolution affects the L-curve elbow of $\eta(m)$ and the resulting data-driven regularity estimate $\tilde{s}(\Omega_z)$. Three reference functions on $\Omega = [-0.5, 0.5]$ are considered: a step function ($H^{0.5-}$), a first-order kink ($H^{1.5-}$), and a second-order kink ($H^{2.5-}$), similar as Figure 2 definition. For each target point z near the low-regularity location, a symmetric local stencil X_z is formed from the n nearest neighbors, with $n \in \{5, \dots, 50\}$ and fixed shape parameter $\varepsilon = 1$.

Figure 9 shows the discrete profiles $\eta(m)$ for increasing n . For the step function, no clear elbow is observed; the profile enters a rapid-growth regime almost immediately across all stencil sizes, reflecting its very low regularity. In contrast, for the first- and second-order kink functions, the profiles appear smooth and lack a distinct elbow when n is very small. A distinct elbow emerges for $n \gtrsim 10$ in the first-order case and $n \gtrsim 15$ in the second-order case. Beyond $n \approx 30$, the estimated $\tilde{s}(\Omega_z)$ stabilizes near the expected regularity. This behavior confirms the data-driven nature of the estimator: when too few samples are available, the local function appears smoother than it actually is, and the estimated $\tilde{s}(\Omega_z)$ overestimates the true $s(\Omega_z)$. As the neighborhood becomes sufficiently informative, $\tilde{s}(\Omega_z)$ converges to $s(\Omega_z)$ from above.

5.2. Example 2: Effect of kernel shape parameter in 1D. We next investigate how the kernel shape parameter ε influences the regularity estimate for the piecewise-smooth function f defined in Appendix A. The function (A.1) contains multiple singularities on $\Omega = [-1, 1]$, including jump discontinuities, a cusp, and a C^1 but not C^2 point, as already illustrated in Figure 3. Experiments use 2000 uniformly spaced samples, $n = 20$ nearest neighbors, and Whittle-Matérn kernels with $\varepsilon \in \{0.6, 0.8, 1.0\}$. The smoothness index m is swept over $(d/2, 5]$. We also test two variable-shape cases $\varepsilon(m) = m$ and $\varepsilon(m) = 1/m$ to illustrate non-constant parame-

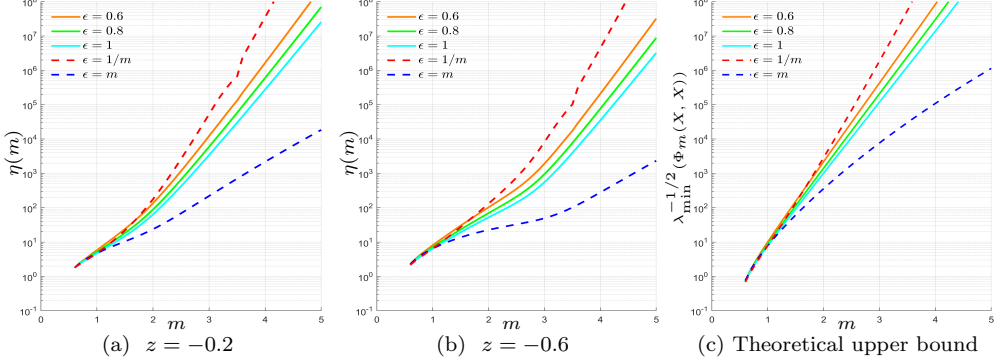


FIG. 10. (*Example 2*) Effect of the shape parameter ε on the norm profiles $\eta(m)$ and the theoretical upper bound $\lambda_{\min}^{-1/2}(\Phi_m(X, X))$ in (2.7), evaluated for the function f (A.1) at the local neighborhoods centered at $z = -0.6$ and $z = -0.2$, using $n=20$ nearest neighbors.

TABLE 1

(*Example 2*) Detected data-driven regularity $\tilde{s}(\Omega_z)$ at selected locations z for the 1D piecewise-smooth test function of Appendix A, using nearest-neighbor stencils of sizes $n = 20$ and $n = 30$ and shape parameters $\varepsilon \in \{0.6, 0.8, 1.0\}$. Smaller ε improves sensitivity to discontinuities and cusps.

location	$z = -0.8$		$z = -0.6$		$z = -0.4$		$z = -0.2$		$z = 0$		$z = 0.5$			
	target s	0.5		2.5		0.5		1.5		0.5		0.5		
		n	20	30	20	30	20	30	20	30	20	30	20	30
$\varepsilon = 1.0$	0.84	0.78	5.00	2.82	0.80	0.74	2.00	1.76	0.86	0.80	0.74	0.64		
$\varepsilon = 0.8$	0.80	0.76	2.92	2.70	0.76	0.72	1.82	1.66	0.82	0.78	0.66	0.64		
$\varepsilon = 0.6$	0.78	0.74	2.76	2.54	0.74	0.72	1.70	1.56	0.78	0.74	0.66	0.64		

terization along the norm-sweep.

Figure 10 illustrates the influence of the kernel shape parameter ε on the discrete norm profiles $\eta(m)$. We focus on two representative locations, $z = -0.6$ and $z = -0.2$, corresponding to local regularities in the sense of $H^{2.5-}$ and $H^{1.5-}$ in f . Smaller ε values produce flatter kernels with broader support, which sharpen the elbow in $\eta(m)$ and improve the detection of local non-smoothness. Larger ε values yield more peaked kernels; their weaker overlap across nodes reduces coupling and makes $\tilde{s}(\Omega_z)$ less responsive to discontinuities. However, excessively small ε also increases the conditioning number of the kernel matrix $\Phi_m(X, X)$, as indicated by the growth of $\lambda_{\min}^{-1/2}(\Phi_m(X, X))$ in the figure. Among the variable-shape cases, $\varepsilon(m) = m$ preserves good conditioning as m increases, whereas $\varepsilon(m) = 1/m$ emphasizes smoothing at large m . These results show that ε need not remain fixed during the m -sweep: moderate adaptation of ε with m can help balance sensitivity to small-scale irregularities against numerical stability.

Table 1 reports the detected data-driven regularity $\tilde{s}(\Omega_z)$ at selected locations for different shape parameters ε and stencil sizes n . At the sampled jump and cusp locations, the expected drops are captured for $\varepsilon = 0.6$, while for $\varepsilon = 1$ the mild C^2 break at $x = -0.6$ is missed. Thus, larger ε flatten the covariance and mask sharp transitions, while smaller ε values yield more accurate yet less stable regularity

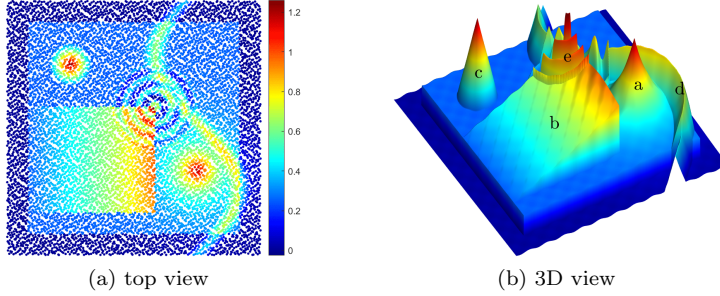


FIG. 11. (*Example 3*) Visualization of the synthetic test function $f(x, y)$ on $\Omega = [0, 6]^2$. Distinct features include cusps, sharp ridges, a cone, curved ridges, and a small oscillatory patch.

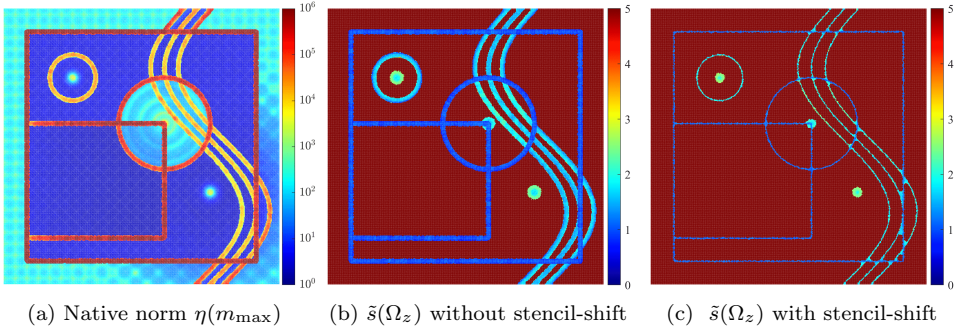


FIG. 12. (*Example 3*) Spatial maps of the native-norm magnitude and data-driven regularity $\tilde{s}(\Omega_z)$ for $f(x, y)$ on $\Omega = [0, 6]^2$ with $n = 50$ and $\varepsilon = 1$.

maps. Comparing $n = 20$ and $n = 30$, the estimates become slightly more stable as n increases, reflecting improved local resolution. Together with the stencil study, these results confirm that $\tilde{s}(\Omega_z)$ converges to $s(\Omega_z)$ from above as data resolution increases and that the kernel covariance, controlled by ε , governs the tightness and stability of the estimate.

5.3. Example 3: Regularity mapping and regularity-limited differentiation on a 2D synthetic function. We apply the proposed Sobolev-scale norm profiling framework to the two-dimensional synthetic test function $f(x, y)$ defined on $\Omega = [0, 6]^2$, see Appendix B for the definition. The function (B.1) combines a smooth oscillatory background with non-smooth structures such as cusps, linear and curved ridges, a cone, and a localized high-frequency disk, see Figure 11.

A total of $N = 160,000$ quasi-random Halton nodes are used, with the same number of uniform evaluation points. At each evaluation point z , a local stencil of $n = 50$ nearest neighbors is selected. For each stencil, the native norm $\eta(m)$ is evaluated using Whittle-Matérn kernels with $\varepsilon = 1$, and $m \in (d/2, 5]$ is swept to obtain the transition order $\tilde{s}(\Omega_z)$.

Figure 12 illustrates the local screening and refinement results. Figure 12a shows the native-norm values $\eta(m_{\max})$, where large magnitudes concentrate near sharp features. Figure 12b displays the initial regularity map without stencil shifting, which already identifies the primary nonsmooth regions and their approximate types through the estimated $\tilde{s}(\Omega_z)$. Figure 12c presents the refined map after stencil shifting, in

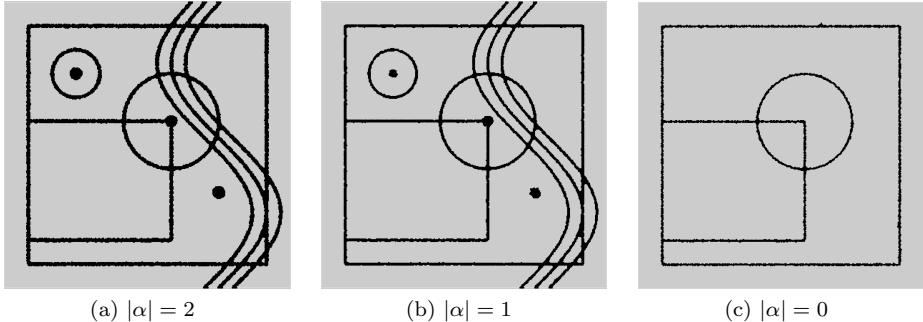


FIG. 13. (*Example 3*) Regions identified by the regularity-limited criterion $\tilde{s}(\Omega_z) \leq |\alpha| + d/2$ for nominal derivative orders (a) $|\alpha| = 2$, (b) $|\alpha| = 1$, and (c) $|\alpha| = 0$, based on adaptive stencil shifting.

which the low-regularity zones become more compact.

To illustrate the practical use of the data-driven regularity, we now view $\tilde{s}(\Omega_z)$ from the perspective of stencil design. In a PDE context, the target differential order $k = |\alpha|$ is known in advance. Regularity screening then identifies locations where the required Sobolev condition $s(\Omega_z) > k + d/2$ is violated. In practice, $\tilde{s}(\Omega_z)$ acts as a spatial reliability map: regions satisfying the condition can support classical k -th order differentiation, while regions where it fails mark zones that require a fallback or regularity-aware stencil strategy.

In the stencil-shift step, we employ an order-dependent interior admissibility margin $\text{dist}(z, \partial \text{conv}(\mathcal{C}_z)) \geq c_{|\alpha|} q_{X_z}$, taking $c_0 = 0$ (interpolation only requires $z \in \text{conv}(\mathcal{C}_z)$) and increasing $c_{|\alpha|}$ with $|\alpha|$ (e.g., one- and two-spacing buffers for first- and second-order operators), and discard candidates that violate this condition. Figure 13 illustrates the regularity-based stencil reliability for different derivative orders and shows the regions flagged for $|\alpha| = 2, 1$, and 0 , respectively. Black areas with $\tilde{s}(\Omega_z) \leq |\alpha| + d/2$ indicate locally insufficient regularity to support accurate RBF-FD differentiation. For $|\alpha| = 2$, most smooth interior points satisfy the condition, whereas for $|\alpha| \leq 1$, only narrow zones near singular features remain excluded. This interpretation recasts the regularity map as a data-driven filter that identifies where finite-difference operators of a chosen order are reliably admissible. After adaptive stencil shifting, the number of flagged points decreases, respectively, from 28,556 to 16,667 for $|\alpha| = 2$, from 28,376 to 11,551 for $|\alpha| = 1$, and from 20,062 to 4,508 for $|\alpha| = 0$, corresponding to reductions of roughly 40%–80% across these cases and yielding a substantially more localized exclusion of low-regularity neighborhoods.

Figure 14 presents the pointwise absolute error maps for the interpolation and differentiation results. Panels (a)–(c) show the reconstructed function f , its first derivative $D_x f$, and the Laplacian Δf , respectively. Errors remain small throughout the smooth regions, while larger values concentrate near the singular features of f . The white contours indicate areas classified as low-regularity, where finite-difference evaluations are intentionally omitted. These results confirm that the regularity-aware refinement preserves accuracy in smooth portions of the domain and correctly isolates regions of limited differentiability.

5.4. Example 4: Regularity mapping and differentiation in turbulent flow data. We demonstrate the applicability of the proposed framework to a real,

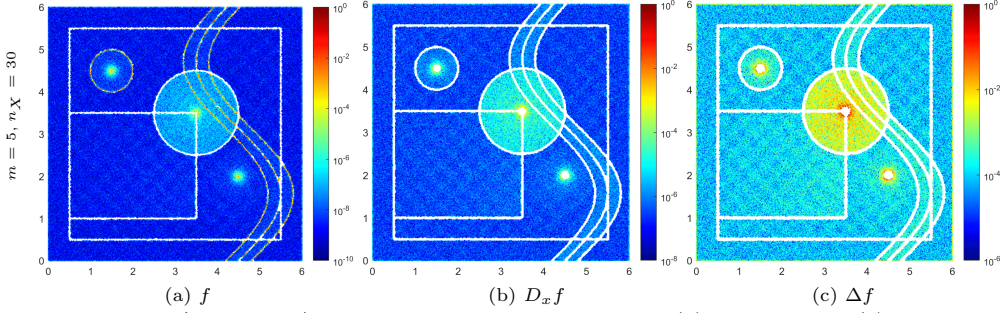


FIG. 14. (*Example 3*) Pointwise absolute error maps for (a) interpolation, (b) x -derivative, and (c) Laplacian on $\Omega = [0, 6]^2$ at 160,000 evaluation points, computed using RBF-FD with $m = 5$.

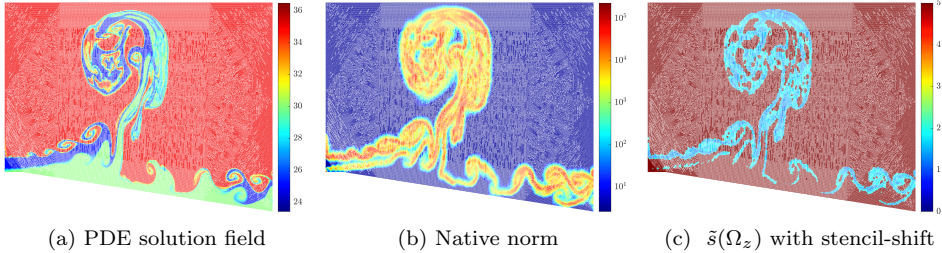


FIG. 15. (*Example 4*) Turbulent-flow dataset on 104,444 scattered nodes. (b) Native-norm with 21,847 outliers identified by IQR-based screening.

non-uniform turbulent flow dataset. The test case is taken from the incompressible-flow benchmark described in Section 2.13 of [19], comprising 104,444 scattered nodes generated by FreeFEM++. The sample distribution is highly irregular due to adaptive meshing in a complex geometry, providing a stringent test of robustness. Throughout this experiment, the local stencil size is fixed at $n = 20$.

Figure 15 illustrates the screening and subsequent regularity analysis. The figure displays (a) the PDE solution field, (b) the native-norm, and (c) the data-driven regularity distribution following adaptive stencil refinement. Irregular spatial sampling leads to elevated native norms near regions of strong gradients, while smooth areas remain clearly separated. After adaptive refinement, the data-driven regularity becomes spatially consistent across the domain.

Using the discrete regularity criterion $\tilde{s}(\Omega_z) < |\alpha| + d/2$, flagged points are classified by the highest derivative order locally supported. Figure 16(a)–(c) show the distributions for $|\alpha| = 2, 1$, and 0 , respectively. The identified regions align with coherent physical structures where flow gradients are steep, while noise and spurious detections in smooth areas are largely suppressed.

Figure 17 compares the derivative reconstruction. Figure 17 (a) shows the FEM reference field $D_x f$, (b) the RBF-FD result using the proposed stencil shifting, and (c) the pointwise difference between them. Across most of the domain, the two fields agree closely, with discrepancies confined to low-regularity and boundary regions.

Quantitative assessment is performed using the FEM reference derivative $D_x f$ field from the benchmark. Figure 17 compares the FEM reference (left), the RBF-FD derivative reconstructed by regularity-aware stencils (center), and their pointwise absolute error (right). Overall agreement is strong, with discrepancies confined to

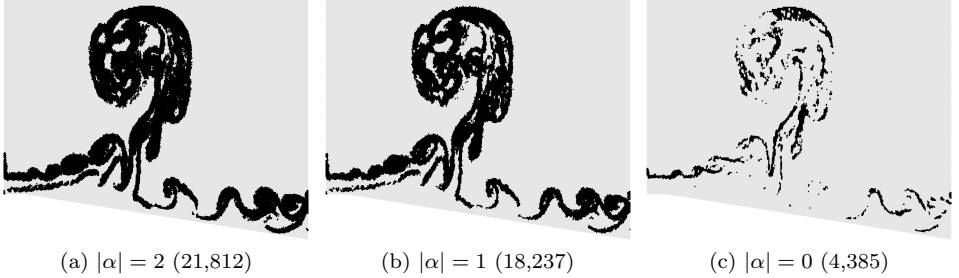


FIG. 16. (*Example 4*) Flagged points under the regularity-limited criterion $\tilde{s}(\Omega_z) < |\alpha| + d/2$ for derivative orders $|\alpha| = 2$, $|\alpha| = 1$, and $|\alpha| = 0$, using adaptive RBF-FD stencils ($n = 20$).

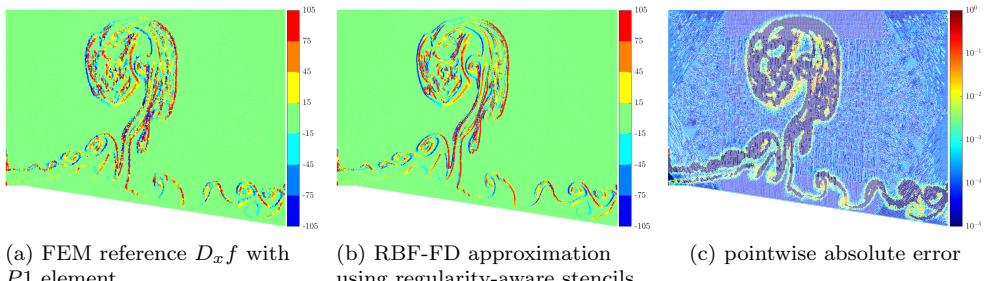


FIG. 17. (*Example 4*) Derivative validation for the turbulent dataset.

low-regularity regions and near boundaries where stencil symmetry is limited.

Near boundaries or strongly irregular regions, high-order finite-difference operators can become ill-conditioned. Following the reliability map, we employ low-order stencils in such regions to maintain stability. More sophisticated treatments, such as adaptive viscosity [20], least-squares RBF-FD [21], or refinement by null rules [22], represent natural extensions. This example demonstrates that the proposed regularity mapping enables stable and accurate differentiation even in non-uniform, physically complex datasets.

6. Conclusion. We have presented a kernel-based framework for quantitative estimation of local Sobolev regularity on scattered data. The approach infers an effective regularity order $\tilde{s}(\Omega_z)$ from the growth of localized native norms as the kernel smoothness parameter m is increased. The resulting Sobolev-scale profiles provide a direct data-driven measure of spatially varying regularity, without requiring any prior knowledge of the underlying function or geometry. A simple transition-based criterion yields $\tilde{s}(\Omega_z)$ efficiently from discrete norm sweeps, while a band-limited surrogate analysis explains the onset of native-norm amplification once the kernel smoothness exceeds the locally resolvable regularity. To enhance spatial selectivity and suppress artifacts due to interface-crossing stencils, an adaptive stencil-shift refinement is incorporated. For large or non-uniform point sets, an accelerated screening strategy concentrates norm evaluations within candidate low-regularity regions and extracts statistically stable tail-based estimates of $\tilde{s}(\Omega_z)$.

Numerical experiments on two-dimensional synthetic benchmarks and turbulent-flow data demonstrate that the method accurately resolves spatially heterogeneous

regularity and retains robustness under severe non-uniform sampling. After stencil refinement, low-regularity features become sharply localized, and derivatives reconstructed via regularity-aware RBF-FD stencils remain stable and well conditioned. These results confirm that $\tilde{s}(\Omega_z)$ serves not only as a diagnostic of local function regularity but also as a quantitative indicator for selecting numerically admissible finite-difference or RBF-FD operators.

In summary, the proposed regularity-profiling framework establishes a unified, data-driven connection between kernel native norms, local Sobolev behavior, and stencil reliability. It provides an effective foundation for adaptive differentiation and regularity-aware PDE discretizations on scattered nodes. Future work will extend this formulation to direct regularity-controlled solvers, optimized boundary and interface treatments, and automated selection of kernel parameters and stencil radii based on local sampling density and estimated smoothness.

Appendix A. 1D test function in Section 5.2. The test function $f(x)$ used in Section 2 and Section 5 is defined on $[-1, 1]$ as

$$(A.1) \quad f(x) = \begin{cases} 0.8, & -1 \leq x < -0.8, \\ 1.2, & -0.8 \leq x < -0.6, \\ 1.2 + 100(x + 0.6)^2, & -0.6 \leq x < -0.4, \\ 5|5x + 1| + 4, & -0.4 \leq x < 0, \\ 6 + 3 \sin(24\pi x), & 0 \leq x < \frac{1}{2}, \\ 2 + \sin(6\pi x), & \frac{1}{2} \leq x \leq 1. \end{cases}$$

Appendix B. 2D test function in Section 5.3. The test function $f(x, y)$ used in Section 5 is defined on $[0, 6]^2$. Let $p_1 = (1.5, 4.5)$, $p_2 = (4.5, 2.0)$, $p_3 = (3.5, 3.5)$ and $r_i = \sqrt{(x - p_{ix})^2 + (y - p_{iy})^2}$ for $i = 1, 2, 3$. Define

$$f_1(x, y) = -0.01 \sin(4\pi x) \cos(4\pi y) + \exp(-2r_2) + 0.2(x + y - 2.75),$$

and set

$$(B.1) \quad f(x, y) = \begin{cases} f_1(x, y), & |x - 2.25| + |y - 2.25| \leq 1.75, \\ 0.4(1 - |x - \sin y - 4.5|/0.3), & |x - \sin y - 4.5| \leq 0.3, \\ 1 - 2r_1, & r_1 \leq 0.5, \\ \frac{1}{2} \sin(20r_3)/(1 + 3r_3), & 2.5 \leq x, y \leq 4.5, r_3 \leq 1, \\ 0.25, & 0.5 \leq x, y \leq 5.5, \\ 0, & \text{otherwise.} \end{cases}$$

REFERENCES

- [1] J. F. CANNY, *A computational approach to edge detection*, IEEE Trans. Pattern Anal. Mach. Intell., PAMI-8 (1986), pp. 679–698.
- [2] S. DE MARCHI, W. ERB, F. MARCHETTI, E. PERRACCHIONE, AND M. ROSSINI, *Shape-driven interpolation with discontinuous kernels: Error analysis, edge extraction, and applications in magnetic particle imaging*, SIAM J. Sci. Comput., 42 (2020), pp. B472–B491.
- [3] S. DE MARCHI, F. MARCHETTI, AND E. PERRACCHIONE, *Jumping with variably scaled discontinuous kernels (VSDKs)*, BIT Num. Math., 60 (2020), pp. 441–463.
- [4] J.-H. JUNG AND V. R. DURANTE, *An iterative adaptive multiquadric radial basis function method for the detection of local jump discontinuities*, Appl. Numer. Math., 59 (2009), pp. 1449–1466.

- [5] J.-H. JUNG, S. GOTTLIEB, AND S. O. KIM, *Iterative adaptive RBF methods for detection of edges in two-dimensional functions*, Appl. Numer. Math., 61 (2011), pp. 77–91.
- [6] G. T. SHRIVAKSHAN AND C. CHANDRAMOULI, *A comparison of various edge detection techniques used in image processing*, Int. J. Comput. Sci. Issues, 9 (2012), p. 269.
- [7] S. MALLAT, *A Wavelet Tour of Signal Processing*, Academic Press, San Diego, 2nd ed., 1999.
- [8] A. HARTEN, B. ENGQUIST, S. OSHER, AND S. R. CHAKRavarthy, *Uniformly high order accurate essentially non-oscillatory schemes, III*, J. Comput. Phys., 71 (1987), pp. 231–303.
- [9] G.-S. JIANG AND C.-W. SHU, *Efficient implementation of weighted ENO schemes*, J. Comput. Phys., 126 (1996), pp. 202–228.
- [10] C. HU AND C.-W. SHU, *Weighted essentially non-oscillatory schemes on triangular meshes*, J. Comput. Phys., 150 (1999), pp. 97–127.
- [11] R. KEMPF AND H. WENDLAND, *High-dimensional approximation with kernel-based multilevel methods on sparse grids*, Numer. Math., 154 (2023), pp. 1–35.
- [12] R. OPFER, *Multiscale kernels*, Adv. Comput. Math., 25 (2006), pp. 357–380.
- [13] H. WENDLAND, *Multiscale analysis in Sobolev spaces on bounded domains*, Numer. Math., 116 (2010), pp. 493–517.
- [14] S. AVESANI, G. GIACCHI, AND M. MULTERER, *Multiresolution local smoothness detection in non-uniformly sampled multivariate signals*, arXiv:2507.13480, (2025).
- [15] H. HARBRECHT AND M. MULTERER, *Samplets: Construction and scattered data compression*, J. Comput. Phys., 471 (2022), p. 111616.
- [16] S. AVESANI, R. KEMPF, M. MULTERER, AND H. WENDLAND, *Multiscale scattered data analysis in samplet coordinates*, arXiv:2409.14791, (2025).
- [17] H. WENDLAND, *Scattered data approximation*, vol. 17, Cambridge University Press, 2004.
- [18] F. J. NARCOWICH, J. D. WARD, AND H. WENDLAND, *Sobolev error estimates and a Bernstein inequality for scattered data interpolation via radial basis functions*, Constr. Approx., 24 (2006), pp. 175–186.
- [19] F. HECHT, *New development in FreeFem++*, J. Numer. Math., 20 (2012), pp. 1–14.
- [20] C. BRACCO, O. DAVYDOV, C. GIANNELLI, AND A. SESTINI, *A positive meshless finite difference scheme for scalar conservation laws with adaptive artificial viscosity driven by fault detection*, Comput. Math. Appl., 190 (2025), pp. 103–121.
- [21] I. TOMINEC, E. LARSSON, AND A. HERYUDONO, *A least squares radial basis function finite difference method with improved stability properties*, SIAM J. Sci. Comput., 43 (2021), pp. A1441–A1471.
- [22] C. BRACCO, F. CALABRÒ, AND C. GIANNELLI, *Discontinuity detection by null rules for adaptive surface reconstruction*, J. Sci. Comput., 97 (2023), p. 37.